



PCCP

**Revealing Reaction Mechanisms of Nanoconfined Li<sub>2</sub>S:  
Implications for Lithium-Sulfur Batteries**

Journal:	<i>Physical Chemistry Chemical Physics</i>
Manuscript ID	CP-ART-03-2018-001462.R1
Article Type:	Paper
Date Submitted by the Author:	30-Mar-2018
Complete List of Authors:	Liu, Z; Hunan Normal University, College of Materials Science and Engineering Deng, Huiqiu; Department of Applied Physics, Hunan University Hu, Wangyu; Department of Applied Physics, Hunan University Gao, Fei; University of Michigan, Michigan, Department of Nuclear Engineering and Radiological Sciences Zhang, Shiguo; Hunan University, College of Materials Science and Engineering Balbuena, Perla; Texas AandM University, Chemical Engineering Mukherjee, Partha; Purdue University College of Engineering, Mechanical Engineering

SCHOLARONE™  
Manuscripts

## Revealing Reaction Mechanisms of Nanoconfined Li<sub>2</sub>S:

### Implications for Lithium-Sulfur Batteries

Zhixiao Liu,<sup>1</sup> Huiqiu Deng,<sup>1,2,\*</sup> Wangyu Hu,<sup>1</sup> Fei Gao,<sup>1,3</sup> Shiguo Zhang,<sup>1</sup> Perla B. Balbuena,<sup>4,\*</sup> Partha P. Mukherjee<sup>5,\*</sup>

<sup>1</sup>College of Materials Science and Engineering, Hunan University, Changsha 410082, China

<sup>2</sup>School of Physics and Electronics, Hunan University, Changsha 410082, China

<sup>3</sup>Department of Nuclear Engineering and Radiological Science, University of Michigan, Ann Arbor, MI 48109, USA

<sup>4</sup>Department of Chemical Engineering, Texas A&M University, College Station, TX 77843, USA

<sup>5</sup>School of Mechanical Engineering, Purdue University, West Lafayette, IN 47907, USA

A manuscript submitted to  
*Phys Chem Chem Phys*  
March, 2018

\*Correspondence: hqdeng@hnu.edu.cn (H. Deng); balbuena@tamu.edu (P. B. Balbuena); pmukherjee@purdue.edu (P. P. Mukherjee)

### Abstract

Using  $\text{Li}_2\text{S}$  as an active material and designing nanostructured cathode hosts are considered as promising strategies to improve the performance of lithium-sulfur (Li-S) batteries. In this study, the reaction mechanisms during delithiation of nanoconfined  $\text{Li}_2\text{S}$  as active material, represented by a  $\text{Li}_{20}\text{S}_{10}$  cluster, are examined by first-principles based calculations and analysis. Local reduction and disproportionation reactions can be observed although the overall delithiation process is an oxidation reaction. Long-chain polysulfides can form as intermediate products; however they may bind to insoluble  $\text{S}^{2-}$  via Li atoms as mediators. Activating the charging process only requires an overpotential of 0.37 V if using  $\text{Li}_{20}\text{S}_{10}$  as the active material. Sulfur allotropes longer than cyclo- $\text{S}_8$  are observed at the end of charge process. Although the discharge voltage of  $\text{Li}_{20}\text{S}_{10}$  is only 1.27 V, it can still deliver an appreciable theoretical energy density of 1480 Wh/kg. This study also suggests that hole polarons, in  $\text{Li}_{20}\text{S}_{10}$  and intermediate products, can serve as carriers to facilitate charge transport. This work provides new insights toward revealing detailed reaction mechanisms of nanoconfined  $\text{Li}_2\text{S}$  as an active material in the Li-S battery cathode.

State-of-art lithium-ion batteries based on the intercalation mechanism encounter a bottleneck blocking the improvement of specific capacity and energy density. Developing rechargeable Li batteries with new electrochemical reaction mechanisms is considered as a promising strategy to significantly improve the performance of the batteries.<sup>1</sup> Great hopes are placed on Li-S batteries because of their high specific energy density (~2600 Wh/kg) and low cost.<sup>2-4</sup> However, the internal “shuttle effect,” which results in an irreversible capacity loss, prevents Li-S batteries from commercialization.

Since the shuttle effect is mainly attributed to the weak chemical interaction between the long-chain polysulfides (PSs) and the surface of the carbonaceous host,<sup>5</sup> great efforts have been conducted to immobilize soluble long-chain PSs by using chemically decorated carbon surfaces<sup>6-8</sup> or polar materials.<sup>9-13</sup> However, a recent mesoscale modeling study pointed out that strong PS/substrate interactions can lead to fast passivation of the cathode surface which also potentially prevented Li-S batteries from achieving high specific capacity.<sup>14</sup>

Using nanostructured host materials to physically trap PSs is another effective method.<sup>15, 16</sup> However, it should be noticed that reducing orthorhombic sulfur ( $\alpha$ -S) to lithium sulfide ( $\text{Li}_2\text{S}$ ) always undergoes enormous volume expansion which consequently leads to mechanical degradation of the cathode host.<sup>17</sup> Xin *et al.* suggested to use smaller  $\text{S}_{2-4}$  molecules confined in the nano-sized pores as active materials for improving specific capacity, cycling stability, and rate capacity.<sup>18</sup> Later, Zhu *et al.* synthesized a sulfur/carbon composite with  $\text{S}_{2-4}$  molecules confined within

0.55 nm pores and found that this cathode retains almost 99.97% capacity per cycle for 1000 cycles at 1 C rate.<sup>19</sup>

Using  $\text{Li}_2\text{S}$  as an active material is a promising method to avoid the mechanical degradation because the first charge cycle which delithiates  $\text{Li}_2\text{S}$  to solid sulfur can generate enough space for tolerating volume expansion in the following discharge cycle. Cui and colleagues found that a voltage barrier around 1 V was required to initiate the charging process of micro-metered  $\text{Li}_2\text{S}$  particles due to their poor conductivity.<sup>20</sup> Decreasing the size of  $\text{Li}_2\text{S}$  particles is expected to enhance the ion and electron transport kinetics. Zhang *et al.* anchored 8.5 nm  $\text{Li}_2\text{S}$  nanoparticles into graphene nanosheets and achieved an initial capacity of 1119 mAh/g with a negligible charge voltage barrier.<sup>21</sup> Hu *et al.* encapsulated 5 nm  $\text{Li}_2\text{S}$  nanocrystals as active material and achieved 0.04% capacity-decayed rate over 1000 cycles.<sup>22</sup>

As discussed above, decreasing the size of active material particles, even to the molecular scale, is a direction to improve the performance of Li–S batteries. To the best of our knowledge, ultra-small  $\text{Li}_2\text{S}$  nanoparticles with sizes smaller than 1 nm have not been experimentally employed in Li–S batteries. The smaller particle size is beneficial for enhancing charge transfer kinetics. Revealing how such a small  $\text{Li}_2\text{S}$  nanoparticle behaves during the delithiation process is critical to evaluate its performance as the active material in the cathode. In this study, we hypothesize that the  $\text{Li}_2\text{S}$  nanoparticle smaller than 1 nm is amorphous because the periodic atom arrangement can be destroyed at this length scale. In addition, previous studies on lithium peroxide ( $\text{Li}_2\text{O}_2$ ) also demonstrated that the amorphous phase possessed faster

charge transfer kinetics.<sup>23, 24</sup> A recent study on sputter-deposited lithium sulfide also demonstrated that the amorphous  $\text{Li}_2\text{S}$  nanofilm as cathode material was more active than the crystalline  $\text{Li}_2\text{S}$  nanofilm in the Li–S battery.<sup>25</sup>

In this study, ultra-small amorphous  $\text{Li}_2\text{S}$  nanoparticles are generated by *ab-initio* molecular dynamics (AIMD) using the Vienna Ab-initio Simulation Package (VASP)<sup>26, 27</sup> based on the density functional theory (DFT)<sup>28, 29</sup> method. The following approach is used to generate ultra-small nanoparticles in the present simulation work:

- (1) Use the melt-and-quench strategy<sup>23</sup> to generate amorphous  $\text{Li}_2\text{S}$  based on a  $(3 \times 3 \times 3)$  crystalline  $\text{Li}_2\text{S}$  supercell (see Figure S1 and detailed discussion in the supporting information).
- (2) Generate a sphere with a diameter of 1 nm at the center of the amorphous  $\text{Li}_2\text{S}$  domain, and then remove atoms out of the sphere. We can obtain a  $\text{Li}_{20}\text{S}_{10}$  cluster at this step.
- (3) Put the  $\text{Li}_{20}\text{S}_{10}$  cluster in a  $20 \times 20 \times 20 \text{ \AA}^3$  cubic box. The cluster is firstly relaxed using AIMD at 300 K for 2 ps with a time step of 2 fs. After the AIMD relaxation, the relaxed structure is then optimized by conventional DFT simulations performed using VASP.

The approach described below is employed to mimic the delithiation process:

- (i) Find four Li atoms which are the most far away from the center of mass of the  $\text{Li}_x\text{S}_{10}$  cluster. Then select two of these four atoms and remove them. We have six different combinations and we will get six  $\text{Li}_{x-2}\text{S}_{10}$  clusters with different configurations.

- (ii) Relax each cluster using AIMD at 300 K for 2 ps with a time step of 2 fs, and then optimize the structure using more accurate DFT simulations.
- (iii) Pick up the  $\text{Li}_{x-2}\text{S}_{10}$  cluster with the lowest total energy and repeat (i) and (ii).

Figure 1(a) shows the atomistic structure of  $\text{Li}_{20}\text{S}_{10}$  cluster after the optimization. In the  $\text{Li}_{20}\text{S}_{10}$  cluster, S atoms only interact with Li atoms, and the S-S bond is not observed. The radius of gyration ( $R_g$ ) is calculated to characterize the size of the cluster as

$$R_g = \sqrt{\frac{\sum_i m_i r_i^2}{\sum_i m_i}}, \quad (1)$$

where  $m_i$  is the mass of the  $i^{\text{th}}$  atom, and  $r_i$  is the distance of the  $i^{\text{th}}$  atom to the center of mass of the cluster. According to Eqn. (1), the  $R_g$  of  $\text{Li}_{20}\text{S}_{10}$  is 3.57 Å. The average Li-S bond in the  $\text{Li}_{20}\text{S}_{10}$  cluster is 2.41 Å, which is shorter than the 2.48 Å Li-S bond length in the crystalline  $\text{Li}_2\text{S}$ .<sup>30</sup> The contracted Li-S bond length makes the radius of the cluster to decrease after the structure optimization. Also, the Li-S bond length in the  $\text{Li}_{20}\text{S}_{10}$  cluster is longer than the 2.11 Å Li-S bond length of the  $\text{Li}_2\text{S}$  molecule.<sup>31</sup> Yu *et al.*<sup>32</sup> also predicted the atomistic structures of  $(\text{Li}_2\text{S})_n$  ( $n = 2\sim 10$ ) clusters using the CALYPSO<sup>33</sup> simulation package, and they also found that the Li-S distances in the  $(\text{Li}_2\text{S})_n$  clusters are longer than the Li-S bond length of the  $\text{Li}_2\text{S}$  molecule. In the crystalline  $\text{Li}_2\text{S}$ , each Li atom is shared by four S atoms. Here we define the coordination number (CN) as the number of S atoms coordinated to a Li atom. In the  $\text{Li}_{20}\text{S}_{10}$  cluster, the average CN is decreased to 2.85. As shown in Figure S2(a), the coordination number will not be less than 2 or larger than 4. 55% of the Li atoms coordinate with three S atoms and only 15% Li

atoms coordinate with four S atoms. Bader analysis<sup>34, 35</sup> is used to understand the charge distribution in the  $\text{Li}_{20}\text{S}_{10}$  cluster, and it is found that the approximate charge of each S is -2.

The binding energy of the  $\text{Li}_{20}\text{S}_{10}$  cluster predicted by combining AIMD and DFT simulations is -0.99 eV as shown in Figure S3 (The details of calculating the binding energy are discussed in the Supporting Information). This value agrees well with the binding energy of the  $\text{Li}_{20}\text{S}_{10}$  cluster predicted by the Yu *et al.*<sup>32</sup> using the CALYPSO<sup>33</sup> simulation package, which is a powerful tool for predicting nanoparticle structures at the atomistic scale.<sup>36, 37</sup>

For the  $\text{Li}_{18}\text{S}_{10}$  cluster, the radius of gyration slightly decreases to 3.51 Å, and the Li-S bond length increases to 2.43 Å. It is interesting to find an  $\text{S}_2$  dimer in the cluster. The S-S bond length of the dimer is 2.16 Å, which is only 0.04 Å longer than the S-S bond in the crystalline  $\text{Li}_2\text{S}_2$  reported by our previous theoretical study.<sup>38</sup> The Bader analysis shows that the net charges on these two S atoms are -0.99 |e| and -1.03 |e|. Hence, the dimer can be considered as a  $\text{S}_2^{2-}$  anion. When the cluster is delithiated to  $\text{Li}_{16}\text{S}_{20}$ , another  $\text{S}_2^{2-}$  anion appears in the cluster as shown in Figure 1(c).

The charging (delithiation) process is always proposed to undergo oxidizing the low order polysulfide (PS) to the high order polysulfide.<sup>39</sup> However, the  $\text{S}_2^{2-}$ -to- $\text{S}^{2-}$  transition is observed when the  $\text{Li}_{16}\text{S}_{10}$  cluster is delithiated to the  $\text{Li}_{14}\text{S}_{10}$  cluster. Comparing Figure 1(d) and Figure 1(c), we can find that the bottom  $\text{S}_2^{2-}$  anion is converted to two  $\text{S}^{2-}$  anions, which indicates that a reduction

reaction happens locally, even though the overall reaction is the oxidation reaction.

At the same time, the top  $S_2^{2-}$  combines with two  $S^{2-}$  anions, resulting in the formation of a  $S_4^{2-}$  anion. At this delithiation step, the local oxidation reaction is



while the local reduction reaction is



Therefore, the overall reaction still yields the charge conversion as:

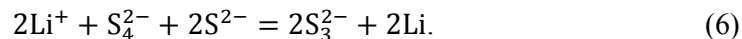


It is worth noting the  $S_4^{2-}$  anion in the  $Li_{16}S_{10}$  cluster is not a chain-like structure as is always found in the organic electrolyte.<sup>40, 41</sup> The  $S_4^{2-}$  anion in the  $Li_{14}S_{10}$  cluster has a branch-like configuration according to our *ab-initio* prediction, and the length of S-S bond is around 2.08 Å. According to the Bader analysis, the net charge of the center S atom in the branch-like  $S_4^{2-}$  is +0.22 |e|, while the net charges of the other three S atoms are -0.68 |e|, -0.76 |e| and -0.78 |e|, respectively.

The conversion of the long PS to the short PS is also observed when the  $Li_{14}S_{10}$  is oxidized to  $Li_{12}S_{10}$ . The sulfur tetramer becomes sulfur trimer as shown in Figure 1(e). According to the Bader analysis, the net charge on the trimer is -1.98 |e|. Hence, a local reduction happens as



In the meantime, another  $S_3^{2-}$  forms at the bottom of the  $Li_{12}S_{10}$  cluster due to the combination of three  $S^{2-}$  ions. The total reaction for the delithiation of  $Li_{14}S_{10}$  to  $Li_{12}S_{10}$  can be written as



As shown in Figure 1(f), a chain-like sulfur tetramer appears at the bottom of the cluster when  $\text{Li}_{12}\text{S}_{10}$  is delithiated to  $\text{Li}_{10}\text{S}_{10}$ . The further delithiation to  $\text{Li}_8\text{S}_{10}$  can convert the other sulfur trimer at the top of the cluster to a sulfur tetramer (Figure 1(g)). The Bader analysis reveals that the ionic states of the tetramers are -2. The S-S bond length in sulfur tetramers is in the range of 2.06-2.09 Å, which is a little shorter than the S-S bond (2.09–2.11 Å) in the isolated  $\text{Li}_2\text{S}_4$  molecule.<sup>31</sup>

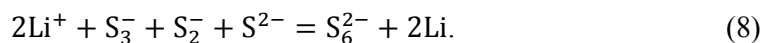
A sulfur dimer and a sulfur trimer appear in the  $\text{Li}_6\text{S}_{10}$  cluster as shown in Figure 1(h). It is important to remark that the ionic states for both the sulfur dimer and sulfur trimer are -1 according to the Bader analysis. Lu *et al.* probed Li-S redox reactions, and they reported that  $\text{S}_3^-$  was not stable in the low-dielectric 1,3-dioxolane:1,2-dimethoxyethane (DOL:DME) solvent.<sup>42</sup> In contrast, Cañas found that  $\text{S}_3^-$  as an intermediate discharge product can be detected in the tetra-ethylene glycol dimethyl ether (TEGDME) solvent at the 25% depth of discharge (roughly related to  $\text{Li}_{0.5}\text{S}$ ).<sup>43</sup> Combining magnetic resonance measurements, X-ray absorption spectroscopy and DFT calculations, Vijayakumar *et al.* studied molecular structures and stabilities of dissolved PSs in the Li-S battery, and they found that the dissociation of  $\text{S}_6^{2-}$  to  $\text{S}_3^-$  was also an exothermic reaction.<sup>40</sup> According to their simulation results, the S-S bond length in  $\text{S}_3^-$  is 2.02Å and the S-S-S bond angle is 116.6°, which are in good agreement with our results. In our current study, the S-S bond length of  $\text{S}_3^-$  in the  $\text{Li}_6\text{S}_{10}$  cluster is about 2.05 Å and the related bond angle is 112.2°. Assary *et al.* systematically studied the reactions in the Li-S battery cathode at

the molecular level using DFT calculations.<sup>44</sup> They found that the formation of  $S_3^-$  and  $S_2^-$  due to the disproportionation of  $S_8^{2-}$  is thermodynamically feasible. They also proposed a disproportionation reaction where a  $S_5^{2-}$  dianion can directly dissociate to  $S_3^-$  and  $S_2^-$  anions although this reaction is endothermic at the molecular level. In our simulation, we found that the disproportionation of  $S_5^{2-}$  to  $S_3^-$  and  $S_2^-$  in the  $Li_6S_{10}$  cluster is an exothermic reaction, and the disproportionation reaction only needs to overcome an energy barrier of 55 meV (Figure S4).

Based on the above discussion, we proposed a reaction path for the formation of  $S_3^-$  and  $S_2^-$  in  $Li_6S_{10}$  cluster as shown in Figure 1(h). During the delithiation process of  $Li_8S_{10}$  to  $Li_6S_{10}$ ,  $S_4^{2-}$  is firstly oxidized to  $S_5^{2-}$  as



Then the  $S_5^{2-}$  dianion decomposes to  $S_3^-$  and  $S_2^-$ . These two anions are not stable and will combine with an  $S^{2-}$  anion to produce  $S_6^{2-}$  at the next-step lithiation, which leads to  $Li_4S_{10}$  as shown in Figure 1(i):



The  $S_6^{2-}$  has a chain-like structure with an S-S bond length varying from 2.04 to 2.09 Å, which agrees well with the 2.09 Å S-S bond length in the  $Li_2S_6$  molecule.<sup>45</sup> Not all S atoms in the hexamer chain are negatively charged. The Bader analysis demonstrated that S atoms coordinating with two Li atoms are charged by -0.82 |e|, while the S atom coordinating with only one Li atom is charged by -0.22 |e|. S atoms which do not interact with Li atoms are almost neutral, with a small negative charge of around 0.05 |e|.

After taking two Li atoms from the original  $\text{Li}_4\text{S}_{10}$  cluster, the  $\text{S}_4^{2-}$  chain and  $\text{S}_6^{2-}$  chain will combine and form a long  $\text{S}_{10}^{2-}$  chain as shown in Figure 1(j). Similarly to the  $\text{S}_6^{2-}$  chain, S atoms without interacting with Li atoms are almost neutral; S atoms coordinating with two Li atoms are charged by  $-0.73 |e|$ ; and S atoms coordinating with one Li atom are charged by  $0.14 |e|$ . It is worth noting that the final charge product is cyclo- $\text{S}_{10}$  as shown in Figure 1(k). The sulfur chemical potential in the  $\text{S}_{10}$  ring is  $-4.08$  eV per atom, which is a little higher than the sulfur chemical potential of  $-4.12$  eV per atom in the crystalline  $\alpha$ -S (packed cyclo- $\text{S}_8$  rings within an orthorhombic structure). The energy difference is only  $40$  meV per atom between the  $\text{S}_{10}$  ring and the  $\text{S}_8$  ring. In addition, the magnitude of  $\kappa T$  ( $\kappa$  represents the Boltzmann constant) is around  $26$  meV at  $T = 300$  K. Hence, we can infer that thermodynamics allows the existence of the cyclo- $\text{S}_{10}$  ring at room temperature. The stability of the  $\text{S}_{10}$  ring is also estimated. It is found that opening the ring is an endothermic reaction requiring an energy of  $1.22$  eV (Figure S5).

Figures 1(a)–(k) describe the atomistic structure evolution during the delithiation process in detail, and the binding energies of these clusters are shown in Figure S3. The negative binding energies indicate that  $\text{Li}_x\text{S}_{20}$  ( $x = 2, 4, 6 \dots 20$ ) clusters are thermodynamically stable. It is interesting to find that the soluble long-chain  $\text{S}_x^{2-}$  ( $x=3, 4, 5, 6$  in this study) is always bonded to insoluble  $\text{S}^{2-}$ . This theoretical finding can be validated by a recent experimental study. Zhang *et al.* investigated the charging mechanism of  $\text{Li}_2\text{S}$  nanoparticles with the size of *ca.*  $500$  nm. They also found that long chain PSs cannot dissolve into the electrolyte during the first charging cycle.<sup>46</sup>

Hence the ultra-small nanoparticle itself can prohibit the dissolution and migration of intermediate products, which leads to alleviating the shuttle effect. As discussed above, the sulfur and  $\text{Li}_2\text{S}$  nanoparticles are always confined in nanostructured host materials.<sup>18, 19, 21</sup> The nanopores can also trap long chain PSs.

The evolution of geometric properties of  $\text{Li}_x\text{S}_{10}$  clusters is summarized in Figure 2. Figure 2(a) demonstrates that the radius of gyration ( $R_g$ ) monotonically decreases during the charge (delithiation) process. Two stages can be identified according to the evolution of  $R_g$ . In each stage,  $R_g$  can be considered as a linear function of the Li content as shown in Figure 2(a). The linear increase of  $R_g$  from the  $\text{S}_{10}$  ring to the  $\text{Li}_{10}\text{S}_{10}$  cluster is larger than that from the  $\text{Li}_{10}\text{S}_{10}$  cluster to the  $\text{Li}_{20}\text{S}_{10}$  cluster. This trend is opposite to the lithiation-induced volume expansion of the bulk phase. Liu *et al.*'s previous theoretical study showed that the lithiation of  $\alpha$ -S to solid  $\text{Li}_2\text{S}_2$  only undergoes 5% volume expansion but the lithiation to crystalline  $\text{Li}_2\text{S}$  experiences 40% volume expansion.<sup>38</sup> The average Li-S distances in different clusters are plotted in Figure 2(b). It is found that  $x = 10$  in  $\text{Li}_x\text{S}_{10}$  is still the critical point in the plot. The average Li-S bond length is always shorter than 2.46 Å in the clusters from  $\text{Li}_{12}\text{S}_{10}$  to  $\text{Li}_{20}\text{S}_{10}$ , while the average bond length suddenly jumps above 2.50 Å when the Li-to-S ratio is below 1:1. It is interesting that the Li-S bond length drops significantly when the  $\text{Li}_8\text{S}_{10}$  cluster is delithiated to the  $\text{Li}_6\text{S}_{10}$  cluster. The decrease in Li-S bond length is attributed to the disproportionation reaction which cleaves a long sulfur chain to two short chains. Our previous theoretical study also found that the Li-S distance in  $\text{Li}_x\text{S}_2$  molecules reduced as the length of the sulfur chain decreased.<sup>47</sup> This trend was

also confirmed by Wang *et al.*'s results.<sup>48</sup>

It is well known that the crystalline Li<sub>2</sub>S has an anti-fluorite structure in which each Li atom coordinates four S atoms (CN = 4).<sup>49</sup> For Li<sub>x</sub>S<sub>10</sub> clusters, the average coordination number of Li is always less than four except for the Li<sub>2</sub>S<sub>10</sub> clusters (Figure 2(c)). As shown in Figure S2, the Li coordination number can sometimes reach five but it never reaches six. In addition, Li atoms need to coordinate with at least two atoms.

The energy profiles during the delithiation process at different applied voltages are estimated and shown in Figure 3.  $U^0 = 1.50$  V is the equilibrium voltage which makes the energies of the redox ends equal:

$$E_{Li_{20}S_{10}} = E_{S_{10}} + 2(\mu_{Li} - eU^0). \quad (9)$$

Eqn (9) can be rewritten as

$$U^0 = -\frac{1}{2e}(g_{Li_2S} - g_S - 2\mu_{Li}). \quad (10)$$

Here  $E_{Li_{20}S_{10}}$  is the energy of a Li<sub>20</sub>S<sub>10</sub> cluster,  $E_{S_{10}}$  is the energy of an S<sub>10</sub> ring and  $\mu_{Li}$  is the energy per Li atom in the body-centered cubic (*bcc*) structure.  $g_{Li_2S}$  is the energy per Li<sub>2</sub>S unit in the Li<sub>20</sub>S<sub>10</sub> cluster, and  $g_S$  is the energy per sulfur atom in the S<sub>10</sub> ring. It is important to notice that the equilibrium voltage for the ultra-small Li<sub>2</sub>S nanoparticle theoretically predicted in this work is about 0.7 eV lower than the equilibrium voltage of bulk Li<sub>2</sub>S.<sup>50,51</sup> The nanometer-sized Li<sub>2</sub>S particle (*e. g.* Li<sub>20</sub>S<sub>10</sub> cluster in this work) always possesses a large specific surface area. As shown in Figure S2, Li and S atoms cannot completely coordinate with each other, and dangling bonds can significantly increase the surface energy. Therefore,  $g_{Li_2S}$  is about 1.1 eV

higher than the chemical potential of  $\text{Li}_2\text{S}$  ( $\mu_{\text{Li}_2\text{S}}$ ) in the antifluorite phase.

As shown in Figure 3,  $U^{\text{ch}} = 1.87 \text{ V}$  is the lowest voltage which makes the energy profile downhill from the fully lithiated state ( $\text{Li}_{20}\text{S}_{10}$ ) to the fully delithiated state ( $\text{S}_{10}$ ); and  $U^{\text{disch}} = 1.26 \text{ V}$  is the highest discharge voltage which can completely convert the  $\text{S}_{10}$  ring to the  $\text{Li}_{20}\text{S}_{10}$  cluster. Although the discharge voltage of  $\text{Li}_{20}\text{S}_{10}$  cathode is much lower than the conventional Li-S batteries, the  $\text{Li}_{20}\text{S}_{10}$  cathode can still deliver a specific energy density about 1480 Wh/kg of  $\text{Li}_2\text{S}$ , which is at least twice as high as the specific energy density of transition-metal based oxides and phosphates.<sup>52</sup> For large-scale applications such as ground transportation and stationary energy storage, the specific capacity, energy density and the cost of fabrication are always considered to be more important than the discharge voltage. Using an atomic layer deposition technique, Meng *et al.* deposited an amorphous  $\text{Li}_2\text{S}$  nanofilm on the copper foil as cathode for Li-S batteries, and they found that the discharge voltage plateau was about 1.7 V.<sup>53</sup> Meng *et al.*'s work also demonstrated that the amorphous  $\text{Li}_2\text{S}$  nanofilm on the Cu foil could exhibit good rate capacities and cycling performance. Xin *et al.* used the nanoconfined smaller  $\text{S}_2$ – $\text{S}_4$  molecules as the active material in the cathode, and they found that these small sulfur allotropes can deliver an energy density of 785 Wh/kg (based on cathode and anode) with a discharge voltage of 1.9 V.<sup>18</sup>

Another key advantage of using ultra-small  $\text{Li}_2\text{S}$  nanoparticles is that the charging process requires a relatively low overpotential. According to the present simulation results, the overpotential of the charging process is 0.37 eV. Cui and collaborators

studied using the micrometer-sized  $\text{Li}_2\text{S}$  particles as the cathode material, and they found that activating the charge (delithiation) process needs to overcome a potential barrier of 1 V due to the poor conductivity of bulk  $\text{Li}_2\text{S}$ .<sup>20</sup> Recently, Cui and colleagues reported that metal sulfides as additives could reduce the potential barrier for activating the charging process. Their results demonstrated that  $\text{TiS}_2$  was the best choice to lower the potential barrier. However, the 2.9 V charge voltage (which corresponds to about 0.6 V overpotential) is still needed to completely convert  $\text{Li}_2\text{S}$  to  $\text{S}_8$ . At the nanometer level, electrons can be transferred by the tunneling effect.<sup>54, 55</sup> The poor conductivity of  $\text{Li}_2\text{S}$  would not be a problem when  $\text{Li}_2\text{S}$  nanoparticles were incorporated into nanostructured host materials with good electronic conductivity. For the crystalline  $\text{Li}_2\text{S}$ , the neutral Li vacancy formation energy is 3.37 eV. This indicates that the charge voltage for extracting Li atoms from bulk  $\text{Li}_2\text{S}$  should be 3.37 V at least.<sup>56</sup>

Our previous studies have demonstrated that hole polarons have the potential to serve as charge carriers in crystalline  $\text{Li}_2\text{S}$  and  $\text{Li}_2\text{S}_2$  to enhance the electronic conductivity of discharge products.<sup>38, 51</sup> Theoretical studies have shown that polarons also play an important role in improving the electronic conductivities of discharge products in Li/Na–air batteries.<sup>23, 57-62</sup> By combining the theoretical and experimental investigations, Nørskov and collaborators found that hole polaron tunneling principally affects the charge transport through  $\text{Li}_2\text{O}_2$  at practical current densities.<sup>55</sup> In crystalline  $\text{Li}_2\text{S}$  and  $\text{Li}_2\text{S}_2$ , the hole polaron hopping distances are 2.86 Å and 4.55 Å, respectively, which are comparable to the size of the  $\text{Li}_x\text{S}_{20}$  cluster. Hence, we

hypothesize that the  $\text{Li}_2\text{S}$  nanoparticle and corresponding intermediate products can transfer charge via polaron tunneling effect.

The Heyd–Scuseria–Ernzerhof (HSE06) hybrid functional is employed to investigate the formation of polarons in  $\text{Li}_x\text{S}_{10}$  clusters.<sup>63</sup> Figure 4 shows the distribution of hole polarons ( $p^+$ ) in  $\text{Li}_x\text{S}_{20}$  clusters. Each cluster is polarized by two polarons (each cluster is positively charged by  $2|e|$ ). According to these findings, the scenario of the charging process can be described as: at each step, the cluster will lose two electrons and generate two hole polarons as shown in Figure 4, and then the extra positive charge can be removed by dissolving two  $\text{Li}^+$  into the electrolyte. On the other hand, during the discharging process, the combination of  $\text{Li}^+$  cations to a  $\text{Li}_x\text{S}_{10}$  cluster can introduce hole polarons into the cluster, and then hole polarons can be eliminated by electrons provided by the carbon cathode substrate.

We also tried to negatively charge these clusters and found that the extra charges were delocalized and electron polarons could not form in these  $\text{Li}_x\text{S}_{10}$  clusters. Using DFT calculations with the HSE06 hybrid functional, Kim *et al.* studied the charged native defects in crystalline  $\text{Li}_2\text{S}$  and reported that the electron polaron can be a potential charge carrier.<sup>64</sup> However, our previous theoretical study demonstrated that the electron polaron was not stable in the crystalline  $\text{Li}_2\text{S}$ .<sup>47</sup> Quite recently, Park *et al.* confirmed that the electron polaron was unstable in crystalline  $\text{Li}_2\text{S}$ .<sup>65</sup> In  $\text{Li}_2\text{S}$ , the  $3p$  orbitals of all S atoms are fully occupied. Therefore, it is difficult for  $\text{S}^{2-}$  to accept another electron to form an electron polaron.<sup>47</sup>

Following the hypothesis discussed above, two electrons are removed from the

original neutral  $\text{Li}_{20}\text{S}_{10}$  cluster at the beginning point of the charging process. According to the spin density depicted in Figure 4(a), it is found that these two extra positive charges are localized on two S atoms, respectively. The ionic states of the corresponding S atoms become -1 according to Bader analysis. For the polarized  $\text{Li}_{20}\text{S}_{10}$  cluster shown in Figure 4(a), the two polarons are localized at two nonadjacent  $\text{S}^{-1}$  anions, and the distance is 6.96 Å. However, removing two electrons from the crystalline  $\text{Li}_2\text{S}$  supercell can generate a  $\text{S}_2^{2-}$  dimer with a bond length around 2.10 Å.<sup>65</sup> Although a  $\text{S}_2^{2-}$  anion appears in the  $\text{Li}_{18}\text{S}_{10}$  cluster, it cannot donate an electron and localize a hole polaron. As shown in Figure 4(b), for the polarized  $\text{Li}_{18}\text{S}_{10}$ , one charge is localized by an S atom in the form of  $\text{S}^{-1}$ , and the other charge is shared by two non-directly interacting S atoms. It is interesting to find that the orientation of the dumbbell-like isosurfaces is parallel to the line between these two S atoms. This feature is similar to the spin density isosurface of the hole polaron in the crystalline  $\text{Li}_2\text{S}_2$ .<sup>38</sup> It is also worth pointing out that the two S atoms sharing one polaron will combine and form  $\text{S}_2^{2-}$  after losing two  $\text{Li}^+$  cations (Figure 1(c)). Figure 4(c) shows the spin density distribution in the polarized  $\text{Li}_{16}\text{S}_{10}$  cluster. In the polarized  $\text{Li}_{16}\text{S}_{10}$ , one positive charge is localized on a S atom, and the other one is localized on the anti-bonding orbital of the dimer. As shown in Figure 1(d), the branch-like tetramer forms in the  $\text{Li}_{14}\text{S}_{10}$  cluster, but the tetramer will not accept polarons. For the polarized  $\text{Li}_{14}\text{S}_{10}$ , one positive charge is localized by an atom; the other charge is shared by two non-directly interacted S atoms, which is similar to the polarized  $\text{Li}_{18}\text{S}_{20}$  (Figure 4(b)). The  $\text{Li}_{12}\text{S}_{10}$  cluster has two  $\text{S}_3^{2-}$  anions (Figure 1(e)), and both

of them can accept the hole polaron as shown in Figure 4(e). The ionic state of the polarized S trimer anion is -1. It is worth noticing that the isosurfaces of the spin density are vertical to the  $S_3$  molecular plane, indicating that one electron from the  $\pi_3^4$  orbital is removed after forming the hole polaron. For other polarized clusters (Figures 4(f)-4(j)), the positive charges are always localized on long-chain polysulfides. Except for the polarized  $Li_2S_{10}$  (Figure 4(j)), each long-chain polysulfide can only accept one positive charge. Figure 1(h) shows that  $S_2^-$  and  $S_3^-$  appear in the neutral  $Li_6S_{10}$  cluster. After losing two electrons,  $S_2^-$  and  $S_3^-$  combine and accept one positive charge as shown in Figure 4(h).

According to the presented theoretical results, this study proposes that the hole polaron formation always happens throughout the entire delithiation process. This hypothesis could be validated by experiments. Hard X-ray photoemission spectroscopy (HAXPES) and electron paramagnetic resonance (EPR) measurements are effective strategies to detect polarons. Combining HAXPES and DFT calculations, Banerjee and collaborators found that Li intercalation can generate polarons in a  $V_2O_5$  nanowire.<sup>66</sup> EPR has been successfully employed to detect the hole polaron ( $O^-$  anion with electronic configuration of  $2p^5$ ) in ZnO.<sup>67</sup> In our simulation, some hole polarons appear as  $S^-$  anions which have the  $3p^5$  configuration and can also act as the paramagnetic center for EPR detecting. Other hole polarons localized in PSs also have the  $1 \mu_B$  magnetic moment, and they can also potentially be mapped by EPR.

In summary, the *ab-initio* simulation method is used to study the delithiation process of ultra-small  $Li_2S$  nanoparticle which is represented by a  $Li_{20}S_{10}$  cluster. It is

interesting to find that although the overall delithiation process is an oxidation reaction, local reduction reactions and disproportionation reactions can be observed. Long-chain PSs can be found in intermediate products. However, these PSs can be firmly bonded to insoluble  $S^{2-}$  via Li atoms as mediators. The charge and discharge voltages are also estimated based on the energy profiles of changing Li content in the cluster. The charge process only requires 0.37 V overpotential. Although the discharge voltage of the  $Li_{20}S_{10}$  particle is only 1.26 V, it can still deliver a theoretical specific energy density about 1480 Wh/kg of  $Li_2S$ . During the charging process, polarons can form in the ultra-small particles, which can provide charges to support electrochemical reactions.

Due to the limitation of the computational resources, the current study only considers the delithiation process of a  $Li_2S$  particle with a sub-nanometer diameter. To the best of our knowledge, how to synthesize such a small  $Li_2S$  nanoparticle has not been achieved by experimental strategies. However, there have been a few experimental efforts demonstrating that sub-nanometer sulfur clusters can be incorporated into the nanoporous carbon frameworks.<sup>18, 19</sup> These pioneering studies perhaps can inspire how to synthesize cathode composites with nanostructured carbon-based frameworks encapsulating ultra-small  $Li_2S$  particles.

This study is the first attempt to probe reactions during the delithiation of an ultra-small  $Li_2S$  nanoparticle, where only an isolated nanoparticle is considered at the current stage. It is still unclear that if small nanoparticles would agglomerate during charging/discharging process. The agglomeration of nanoparticles can increase the

charge transport distance and slow down the kinetics. In addition, the electrolyte also plays a significant role in the Li-S electrochemical system. An interesting and important remaining question is whether side reactions may happen between the electrolyte and the nanoparticle, and then result in chemical degradation. Investigating the inter-particle interplay and the particle-electrolyte interplay is planned as future studies to answer these questions.

### Computational Methods

All simulations presented in this work were performed on VASP.<sup>26, 27</sup> The projector augmented-wave (PAW)<sup>68, 69</sup> method was used to describe the ion-electron interaction, and the electron-electron exchange correlations were described by the Perdew-Burke-Ernzerhof (PBE) functional.<sup>70</sup> For all DFT calculations, the energy cutoff of plane wave basis sets was set to 400 eV, and the residual force for relaxing atom positions was less than 0.02 eV/Å. For all AIMD simulations, the cutoff energy was set to 250 eV. AIMD simulations were carried out with *NVT* ensemble. The Nosé-thermostat<sup>71</sup> with a mass of  $\sim 50 \text{ amu} \cdot \text{Å}^2$  (SMASS=0.30)<sup>23</sup> was used to control the temperature oscillation. The purpose of the AIMD simulation with small cutoff energy and large time step is conducting the relatively rough structure relaxation. After the AIMD simulation, the DFT simulation with 400 eV cutoff energy is conducted to refine the nanoparticle structure. Spin polarization was considered in all simulations. Only the  $\Gamma$ -point was sampled in the Brillouin zone.

### Supporting Information

Details of melt-and-quench approach; population of coordination numbers for Li atoms; conformations of closed  $S_{10}$  and opened  $S_{10}$ .

### **Conflicts of Interest**

There are no conflicts of interest to declare.

### **Acknowledgements**

This work is financially supported by National Natural Science Foundation of China (grant numbers: 51771073, 51772089) and the Assistant Secretary for Energy Efficiency and Renewable Energy, Office of Vehicle Technologies of the U.S. Department of Energy with Contract No. DE-EE0006832 under the Advanced Battery Materials Research (BMR) Program. This material is also based upon work supported by the U.S. Department of Energy's Office of Energy Efficiency and Renewable Energy (EERE), as part of the Battery 500 Consortium, Award Number DE-EE0008210. Z. Liu is thankful for the research start-up funding from Hunan University. Computational resources provided by National Supercomputing Center in Changsha is gratefully acknowledged. The authors thank Dr. Zhenhua Zeng (Purdue University) for useful discussions.

### **References**

1. P. G. Bruce, S. A. Freunberger, L. J. Hardwick and J.-M. Tarascon, *Nature Materials*, 2012, 11, 19-29.
2. Y.-X. Yin, S. Xin, Y.-G. Guo and L.-J. Wan, *Angewandte Chemie-International Edition*, 2013, 52, 13186-13200.
3. Y. Son, J.-S. Lee, Y. Son, J.-H. Jang and J. Cho, *Advanced Energy Materials*, 2015, 5.

4. Q. Pang, X. Liang, C. Y. Kwok and L. F. Nazar, *Nature Energy*, 2016, 1.
5. Q. Zhang, Y. Wang, Z. W. Seh, Z. Fu, R. Zhang and Y. Cui, *Nano Letters*, 2015, 15, 3780-3786.
6. R. Carter, D. Ejorh, K. Share, A. P. Cohn, A. Douglas, N. Muralidharan, T. M. Tovar and C. L. Pint, *Journal of Power Sources*, 2016, 330, 70-77.
7. T.-Z. Hou, X. Chen, H.-J. Peng, J.-Q. Huang, B.-Q. Li, Q. Zhang and B. Li, *Small*, 2016, 12, 3283-3291.
8. F. Pei, T. An, J. Zang, X. Zhao, X. Fang, M. Zheng, Q. Dong and N. Zheng, *Advanced Energy Materials*, 2016, 6.
9. B. Cao, Y. Chen, D. Li, L. Yin and Y. Mo, *ChemSuschem*, 2016, 9, 3338-3344.
10. X. Chen, H.-J. Peng, R. Zhang, T.-Z. Hou, J.-Q. Huang, B. Li and Q. Zhang, *Acs Energy Letters*, 2017, 2, 795-801.
11. W. Kong, L. Yan, Y. Luo, D. Wang, K. Jiang, Q. Li, S. Fan and J. Wang, *Advanced Functional Materials*, 2017, 27.
12. H. Al Salem, G. Babu, C. V. Rao and L. M. R. Arava, *Journal of the American Chemical Society*, 2015, 137, 11542-11545.
13. G. Babu, N. Masurkar, H. Al Salem and L. M. R. Arava, *Journal of the American Chemical Society*, 2017, 139, 171-178.
14. Z. Liu and P. P. Mukherjee, *ACS Applied Materials & Interfaces*, 2017, 9, 5263-5271.
15. Y. Yang, G. Zheng and Y. Cui, *Chemical Society Reviews*, 2013, 42, 3018-3032.
16. H. Chen, Y. Shen, C. Wang, C. Hu, W. Lu, X. Wu and L. Chen, *Journal of The Electrochemical Society*, 2018, 165, A6034-A6042.

17. P. Barai, A. Mistry and P. P. Mukherjee, *Extreme Mechanics Letters*, 2016, 9, 359-370.
18. S. Xin, L. Gu, N.-H. Zhao, Y.-X. Yin, L.-J. Zhou, Y.-G. Guo and L.-J. Wan, *Journal of the American Chemical Society*, 2012, 134, 18510-18513.
19. Q. Zhu, Q. Zhao, Y. An, B. Anasori, H. Wang and B. Xu, *Nano Energy*, 2017, 33, 402-409.
20. Y. Yang, G. Zheng, S. Misra, J. Nelson, M. F. Toney and Y. Cui, *Journal of the American Chemical Society*, 2012, 134, 15387-15394.
21. K. Zhang, L. J. Wang, Z. Hu, F. Y. Cheng and J. Chen, *Scientific Reports*, 2014, 4.
22. C. Hu, H. Chen, Y. Xie, L. Fang, J. Fang, J. Xu, H. Zhao and J. Zhang, *Journal of Materials Chemistry A*, 2016, 4, 18284-18288.
23. F. Tian, M. D. Radin and D. J. Siegel, *Chemistry of Materials*, 2014, 26, 2952-2959.
24. Y. L. Zhang, Q. H. Cui, X. M. Zhang, W. C. McKee, Y. Xu, S. G. Ling, H. Li, G. M. Zhong, Y. Yang and Z. Q. Peng, *Angewandte Chemie-International Edition*, 2016, 55, 10717-10721.
25. M. J. Klein, G. M. Veith and A. Manthiram, *Journal of the American Chemical Society*, 2017, 139, 10669-10676.
26. G. Kresse and J. Furthmüller, *Computational Materials Science*, 1996, 6, 15-50.
27. G. Kresse and J. Hafner, *Physical Review B*, 1993, 48, 13115-13118.
28. R. Car and M. Parrinello, *Physical Review Letters*, 1985, 55, 2471-2474.
29. R. O. Jones and O. Gunnarsson, *Reviews of Modern Physics*, 1989, 61, 689-746.
30. Z. Liu, D. Hubble, P. B. Balbuena and P. P. Mukherjee, *Physical Chemistry Chemical*

- Physics*, 2015, 17, 9032-9039.
31. Z. Liu, P. B. Balbuena and P. P. Mukherjee, *Journal of Coordination Chemistry*, 2016, 69, 2090-2105.
  32. T. Yu, F. Li, C. Liu, S. Zhang, H. Xu and G. Yang, *Journal of Materials Chemistry A*, 2017, 5, 9293-9298.
  33. Y. Wang, J. Lv, L. Zhu and Y. Ma, *Physical Review B*, 2010, 82, 094116.
  34. M. Yu and D. R. Trinkle, *Journal of Chemical Physics*, 2011, 134.
  35. W. Tang, E. Sanville and G. Henkelman, *Journal of Physics-Condensed Matter*, 2009, 21.
  36. J. Lv, Y. Wang, L. Zhu and Y. Ma, *Nanoscale*, 2014, 6, 11692-11696.
  37. S. Li, X. Zhao, X. Xu, Y. Gao and Z. Zhang, *Physical review letters*, 2013, 111, 115501.
  38. Z. Liu, P. B. Balbuena and P. P. Mukherjee, *The Journal of Physical Chemistry Letters*, 2017, 8, 1324-1330.
  39. D.-W. Wang, Q. Zeng, G. Zhou, L. Yin, F. Li, H.-M. Cheng, I. R. Gentle and G. Q. M. Lu, *Journal of Materials Chemistry A*, 2013, 1, 9382-9394.
  40. M. Vijayakumar, N. Govind, E. Walter, S. D. Burton, A. Shukla, A. Devaraj, J. Xiao, J. Liu, C. Wang, A. Karim and S. Thevuthasan, *Physical Chemistry Chemical Physics*, 2014, 16, 10923-10932.
  41. L. E. Camacho-Forero, T. W. Smith, S. Bertolini and P. B. Balbuena, *The Journal of Physical Chemistry C*, 2015, 119, 26828-26839.
  42. Y.-C. Lu, Q. He and H. A. Gasteiger, *The Journal of Physical Chemistry C*, 2014, 118,

5733-5741.

43. N. A. Cañas, D. N. Fronczek, N. Wagner, A. Latz and K. A. Friedrich, *The Journal of Physical Chemistry C*, 2014, 118, 12106-12114.
44. R. S. Assary, L. A. Curtiss and J. S. Moore, *The Journal of Physical Chemistry C*, 2014, 118, 11545-11558.
45. L. J. Wang, T. R. Zhang, S. Q. Yang, F. Y. Cheng, J. Liang and J. Chen, *J. Energy Chem.*, 2013, 22, 72-77.
46. L. Zhang, D. Sun, J. Feng, E. J. Cairns and J. Guo, *Nano Letters*, 2017, 17, 5084-5091.
47. Z. Liu, P. B. Balbuena and P. P. Mukherjee, *Journal of Coordination Chemistry*, 2016, 69, 2090-2105.
48. L. Wang, T. Zhang, S. Yang, F. Cheng, J. Liang and J. Chen, *Journal of Energy Chemistry*, 2013, 22, 72-77.
49. W. Buehrer, F. Altorfer, J. Mesot, H. Bill, P. Carron and H. G. Smith, *Journal of Physics: Condensed Matter*, 1991, 3, 1055-1064.
50. R. Xu, J. Lu and K. Amine, *Advanced Energy Materials*, 2015, 5, n/a-n/a.
51. Z. Liu, P. B. Balbuena and P. P. Mukherjee, *The Journal of Physical Chemistry C*, 2017, 121, 17169-17175.
52. G. Hautier, A. Jain, S. P. Ong, B. Kang, C. Moore, R. Doe and G. Ceder, *Chemistry of Materials*, 2011, 23, 3495-3508.
53. X. Meng, D. J. Comstock, T. T. Fister and J. W. Elam, *Acs Nano*, 2014, 8, 10963-10972.

54. M. D. Radin, C. W. Monroe and D. J. Siegel, *The Journal of Physical Chemistry Letters*, 2015, 6, 3017-3022.
55. A. C. Luntz, V. Viswanathan, J. Voss, J. B. Varley, J. K. Nørskov, R. Scheffler and A. Speidel, *The Journal of Physical Chemistry Letters*, 2013, 4, 3494-3499.
56. G. Luo, J. Zhao and B. Wang, *Journal of Renewable and Sustainable Energy*, 2012, 4.
57. J. M. Garcia-Lastra, J. S. G. Myrdal, R. Christensen, K. S. Thygesen and T. Vegge, *The Journal of Physical Chemistry C*, 2013, 117, 5568-5577.
58. S. Li, J. Liu and B. Liu, *Chemistry of Materials*, 2017, 29, 2202-2210.
59. S. P. Ong, Y. Mo and G. Ceder, *Physical Review B*, 2012, 85, 081105.
60. M. D. Radin, C. W. Monroe and D. J. Siegel, *Chemistry of Materials*, 2015, 27, 839-847.
61. R. B. Araujo, S. Chakraborty and R. Ahuja, *Physical Chemistry Chemical Physics*, 2015, 17, 8203-8209.
62. S. Yang and D. J. Siegel, *Chemistry of Materials*, 2015, 27, 3852-3860.
63. A. V. Krukau, O. A. Vydrov, A. F. Izmaylov and G. E. Scuseria, *Journal of Chemical Physics*, 2006, 125.
64. B. Kim, M. Lee, K. Y. Park and K. Kang, *Chemistry—An Asian Journal*, 2016, 11, 1288-1292.
65. H. Park, N. Kumar, M. Melander, T. Vegge, J. M. Garcia Lastra and D. J. Siegel, *Chemistry of Materials*, 2017.
66. L. R. De Jesus, G. A. Horrocks, Y. Liang, A. Parija, C. Jaye, L. Wangoh, J. Wang, D. A. Fischer, L. F. J. Piper, D. Prendergast and S. Banerjee, *Nature Communications*,

2016, 7, 12022.

67. S. Parashar, B. Murty, S. Repp, S. Weber and E. Erdem, *Journal of Applied Physics*, 2012, 111, 113712.
68. P. E. Blochl, *Physical Review B (Condensed Matter)*, 1994, 50, 17953-17979.
69. X.-G. Xiong and T. Yanai, *Journal of Chemical Theory and Computation*, 2017, 13, 3236-3249.
70. J. P. Perdew, K. Burke and M. Ernzerhof, *Physical Review Letters*, 1996, 77, 3865-3868.
71. S. Nose, *Journal of Chemical Physics*, 1984, 81, 511-519.

### Figure List

**Figure 1.** Evolution of atomistic structure during the delithiation process from  $\text{Li}_{20}\text{S}_{10}$  to  $\text{S}_{10}$ . The violet spheres represent Li atoms, the yellow spheres represent the single S atoms, the green spheres represent the S atoms in dimers, the blue spheres represent the S atoms in trimers, the red spheres represent S atoms in tetramers, the gray spheres represent S atoms in hexamers, and the orange spheres represent S atoms in  $\text{S}_{10}$  chains.

**Figure 2.** Geometric properties of  $\text{Li}_x\text{S}_{10}$  clusters. (a) Radius of gyration, (b) average Li-S bond length and (c) average number of S atoms coordinated to Li.

**Figure 3.** Energy profiles for delithiation/lithiation at different applied voltages versus  $\text{Li}^+/\text{Li}$ .

**Figure 4.** Atomistic structures and spin density distribution of polarized (a)  $\text{Li}_{20}\text{S}_{10}$ , (b)  $\text{Li}_{18}\text{S}_{10}$ , (c)  $\text{Li}_{16}\text{S}_{10}$ , (d)  $\text{Li}_{14}\text{S}_{10}$ , (e)  $\text{Li}_{12}\text{S}_{10}$ , (f)  $\text{Li}_{10}\text{S}_{10}$ , (g)  $\text{Li}_8\text{S}_{10}$ , (h)  $\text{Li}_6\text{S}_{10}$ , (i)  $\text{Li}_4\text{S}_{10}$  and (j)  $\text{Li}_2\text{S}_{10}$ . The violet spheres represent Li atoms, the yellow spheres represent the single S atoms, the green spheres represent the S atoms in dimers, the blue spheres represent the S atoms in trimers, the red spheres represent S atoms in tetramers, the white gray spheres represent S atoms in pentamers, the dark gray spheres represent S atoms in hexamers, and the orange spheres represent S atoms in  $\text{S}_{10}$  chains. The cyan isosurfaces represent the distribution of the net spin density generated by hole polarons.

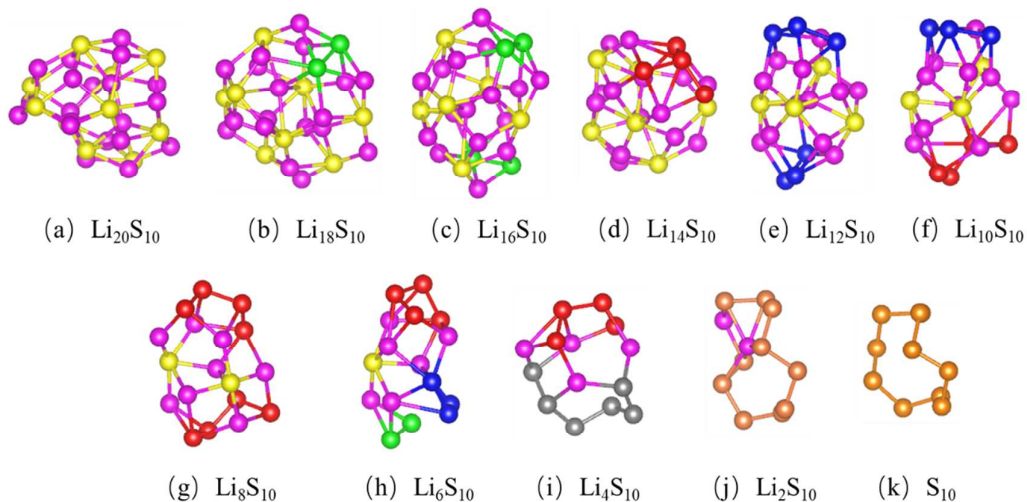


**Figure 1.** Evolution of atomistic structure during the delithiation process from  $\text{Li}_{20}\text{S}_{10}$  to  $\text{S}_{10}$ . The violet spheres represent Li atoms, the yellow spheres represent the single S atoms, the green spheres represent the S atoms in dimers, the blue spheres represent the S atoms in trimers, the red spheres represent S atoms in tetramers, the dark gray spheres represent S atoms in hexamers, and the orange spheres represent S atoms in  $\text{S}_{10}$  chains.

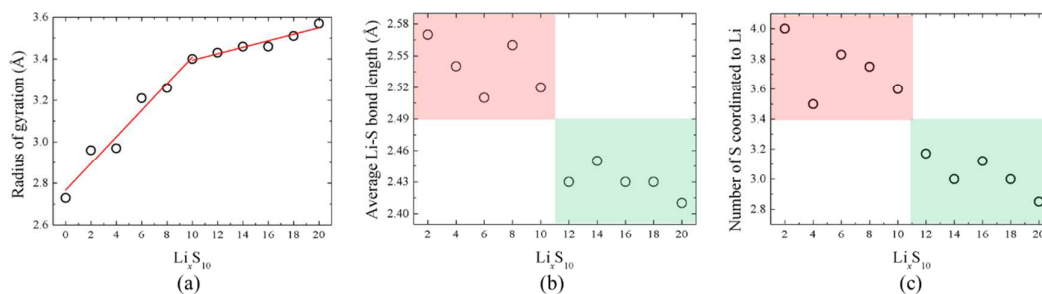


**Figure 2.** Geometric properties of  $\text{Li}_x\text{S}_{10}$  clusters. (a) Radius of gyration, (b) average Li-S bond length and (c) average number of S atoms coordinated to Li.

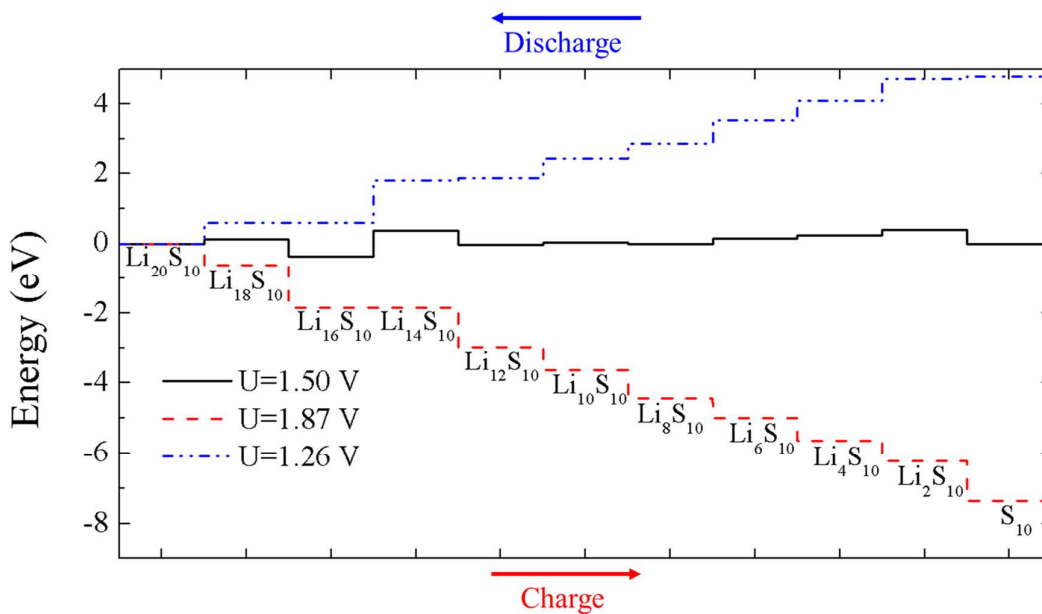


**Figure 3.** Energy profiles for delithiation/lithiation at different applied voltages versus  $\text{Li}^+/\text{Li}$ .

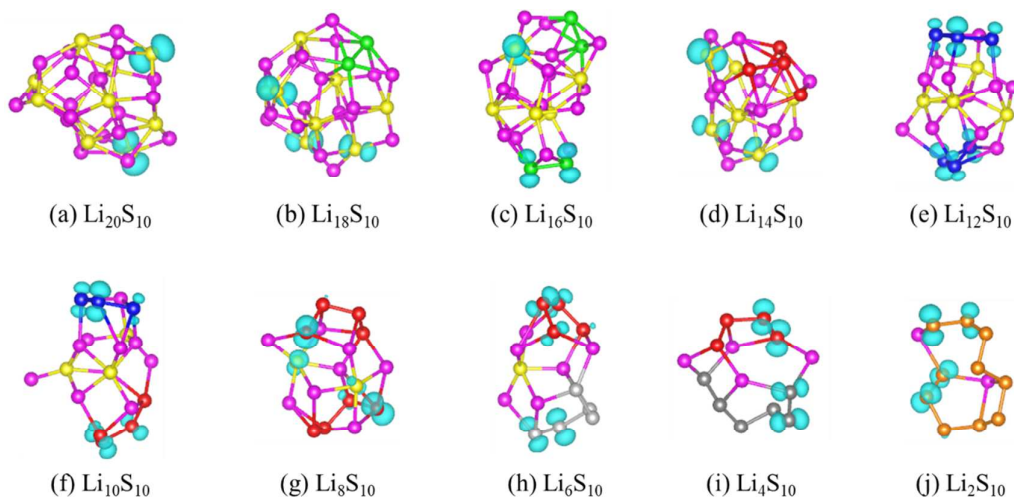


**Figure 4.** Atomistic structures and spin density distribution of polarized (a)  $\text{Li}_{20}\text{S}_{10}$ , (b)  $\text{Li}_{18}\text{S}_{10}$ , (c)  $\text{Li}_{16}\text{S}_{10}$ , (d)  $\text{Li}_{14}\text{S}_{10}$ , (e)  $\text{Li}_{12}\text{S}_{10}$ , (f)  $\text{Li}_{10}\text{S}_{10}$ , (g)  $\text{Li}_8\text{S}_{10}$ , (h)  $\text{Li}_6\text{S}_{10}$ , (i)  $\text{Li}_4\text{S}_{10}$  and (j)  $\text{Li}_2\text{S}_{10}$ . The violet spheres represent Li atoms, the yellow spheres represent the single S atoms, the green spheres represent the S atoms in dimers, the blue spheres represent the S atoms in trimers, the red spheres represent S atoms in tetramers, the white gray spheres represent S atoms in pentamers, the dark gray spheres represent S atoms in hexamers, and the orange spheres represent S atoms in  $\text{S}_{10}$  chains. The cyan isosurfaces represent the distribution of the net spin density generated by hole polarons.